Two-Dimensional Boron Monolayer Sheets

Xiaojun Wu,[†,⊥,*] Jun Dai,[‡,⊥] Yu Zhao,[‡] Zhiwen Zhuo,[†] Jinlong Yang,[§] and Xiao Cheng Zeng[‡,§,*]

[†]CAS Key Lab of Materials for Energy Conversion, Department of Materials Science and Engineering and Hefei National Lab for Physical Materials at Microscale, University of Science and Technology of China, Hefei, Anhui 230026, China, [‡]Department of Chemistry and Nebraska Center for Materials and Nanoscience, University of Nebraska—Lincoln, Lincoln, Nebraska 68588, United States, and [§]Department of Chemical Physics and Hefei National Lab for Physical Science at Microscale, University of Science and Technology of China, Hefei, Anhui 230026, China. [⊥]These authors contributed equally to this work.

ABSTRACT

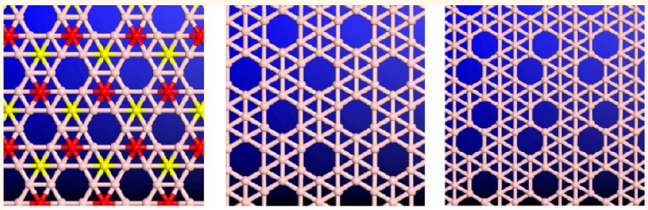

Boron, a nearest-neighbor of carbon, is possibly the second element that can possess free-standing flat monolayer structures, evidenced by recent successful synthesis of single-walled and multiwalled boron nanotubes (MWBNTs). From an extensive structural search using the first-principles particle-swarm optimization (PSO) global algorithm, two boron monolayers (α_1- and β_1-sheet) are predicted to be the most stable α- and β-types of boron sheets, respectively. Both boron sheets possess greater cohesive energies than the state-of-the-art two-dimensional boron structures (by more than 60 meV/atom based on density functional theory calculation using PBE0 hybrid functional), that is, the α-sheet previously predicted by Tang and Ismail-Beigi and the $g_{1/8}$- and $g_{2/15}$-sheets (both belonging to the β-type) recently reported by Yakobson and co-workers. Moreover, the PBE0 calculation predicts that the α-sheet is a semiconductor, while the α_1-, β_1-, $g_{1/8}$-, and $g_{2/15}$-sheets are all metals. When two α_1 monolayers are stacked on top each other, the bilayer α_1-sheet remains flat with an optimal interlayer distance of ~3.62 Å, which is close to the measured interlayer distance (~3.2 Å) in MWBNTs.

KEYWORDS: boron monolayer sheet · hybrid density functional · interlayer distance · double-walled boron nanotube

Among known elements in nature, few can exhibit multiple forms of low-dimensional allotropic structures, such as quasi-0D cage molecules, quasi-1D nanotubes, or quasi-2D sheets. Carbon is an exception as all three low-dimensional allotropes of carbon, including 0D fullerenes,[1] 1D carbon nanotubes,[2] and 2D graphene monolayer sheet,[3] have been isolated in the laboratory. In fact, graphene, a monolayer of carbon with a honeycomb lattice structure, is the first planar (*i.e.*, unbuckled) sheet revealed in nature. A rising question is whether there are other elements in nature that can possess free-standing monolayer allotropes. Silicon, one of nearest-neighbors of carbon in the periodic table, cannot exhibit stand-alone unbuckled monolayer structure due to the tendency of forming sp^3-hybridized Si bonds. To date, free-standing quasi-0D and -1D allotropes of silicon have not been isolated in the laboratory. Many experimental studies and *ab initio* calculations have shown that hollow cages of silicon are unstable, although some small-sized cages can be stabilized by an endohedral metal atom or a metal cluster.[4−7] Likewise, single-walled silicon nanotube can be stabilized by an endohedral metal chain[8] or can form within a cylindrical nanopore.[9] Moreover, although a free-standing monolayer of silicon (*e.g.*, silicene) is unlikely flat, bilayer hexagonal silicon has been predicted to be flat and the planar structure can be a metastable structure and can form within a slit nanopore as suggested from a previous classical molecular dynamics simulation.[10]

Boron is possibly the second element that can possess multiple low-dimensional allotropes. Indeed, previous theoretical predictions by Boustani[11,12] suggested that small-sized boron clusters exhibit quasi-planar structures, which were later confirmed experimentally by Wang, Boldyrev, and their co-workers.[13−17] These studies have motivated increasing interests in seeking new nanostructures of boron, such as boron cage molecules (or boron fullerenes).[18−24] An early prediction[25,26] of the structural transition from quasi-planar to double-ring tubular structures for small-sized boron clusters has also been confirmed by experiments or by high-level *ab initio* calculations.[27−29] The most important experimental evidence of the existence of a low-dimensional allotrope of boron is the successful

* Address correspondence to xzeng1@unl.edu, xjwu@ustc.edu.cn.

Received for review June 18, 2012 and accepted July 15, 2012.

Published online July 20, 2012
10.1021/nn302696v

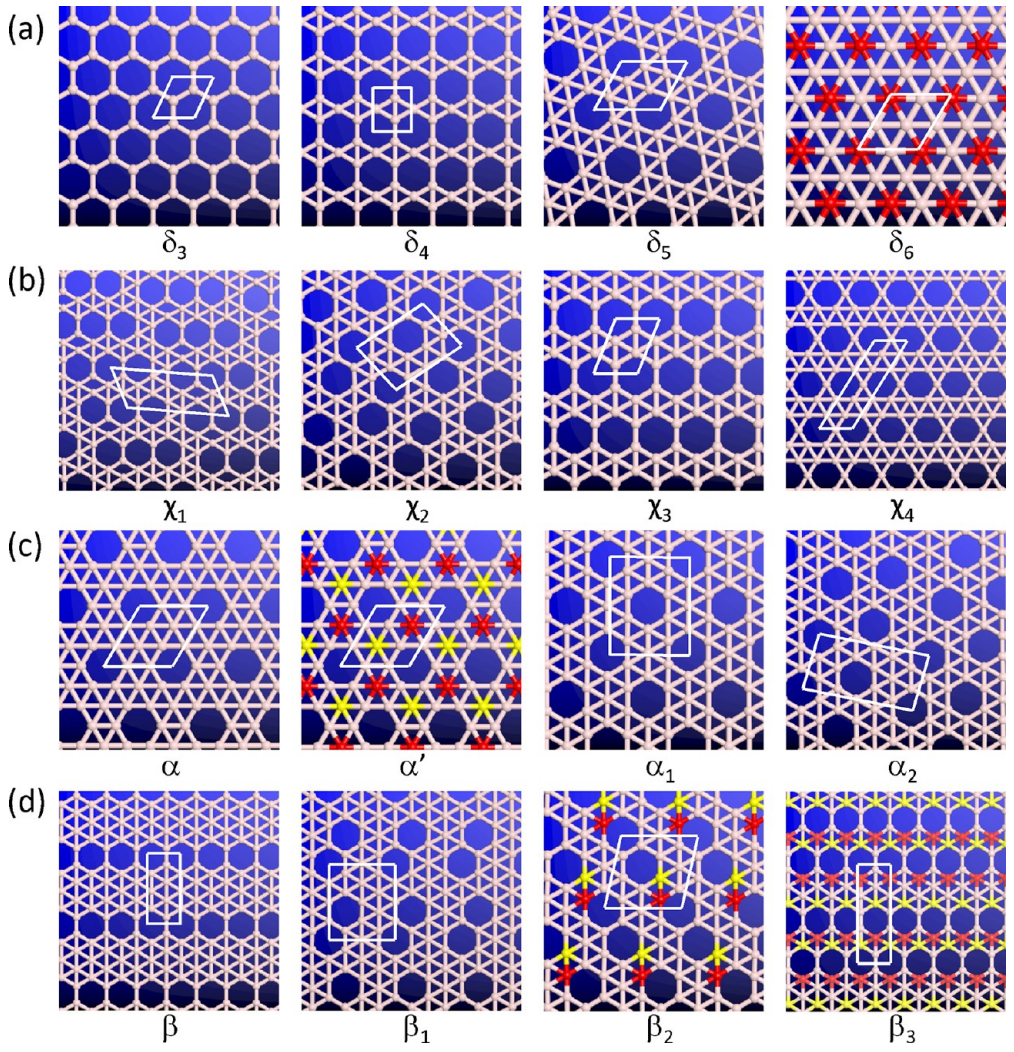

Figure 1. Top view of various low-energy structures of (a) δ-, (b) χ-, (c) α-, and (d) β-type boron monolayer sheets. Red and yellow balls denote boron atoms moving outward or inward from the plane, resulting in buckled boron sheets.

synthesis of single-walled boron nanotubes (SWBNTs) and multiwalled boron nanotubes (MWBNTs).[30,31] In particular, high-resolution transmission electron microscopy (HRTEM) experiments have revealed that the spacing between two adjacent layers of MWBNTs is about 3.2 Å.[31] Furthermore, previous experimental measurement and theoretical calculation have shown that the BNTs are highly conductive,[31,32] indicating that boron sheets, if they exist, are likely metallic. Like carbon nanotubes (CNTs), a SWBNT can be viewed as rolling up a boron monolayer sheet, while a MWBNT can be viewed as rolling up a multilayered sheet. To date, the exact atomic structure of the boron monolayer sheet has not been determined from experiments, except an indirect evidence of the interlayer distance within MWBNTs being 3.2 Å. The latter suggests that the interlayer interaction is likely van der Waals (vdW) type rather than covalent. Nevertheless, various crystalline structures of buckled and unbuckled monolayer structures of boron, which include the α-sheet,[33−35] β-sheet,[33,34] γ-sheet,[36] $g_{1/8}$- and $g_{2/15}$-sheets (see below),[37] triangular sheet, or graphene-like hexagonal sheet, have been predicted from previous *ab initio* computations. All of these boron sheets can be constructed by carving different patterns of heagonal holes within the triangular sheet, and their area densities can be described by a global density parameter, η,[33,34] which is defined as the ratio of number of hexagon holes to the number of atomic sites in the pristine triangular sheet within a unit cell of the decorated boron sheet. Among all of the boron monolayer sheets reported thus far, Tang and Ismail-Beigi[33,34] showed that the α-sheet (with a value of η = 1/9) is possibly the best candidate for the most stable boron monolayer sheet because it has the greatest cohesive energy per atom (in DFT calculation) than other monolayer sheets. Recently, Yakobson and co-workers demonstrated through a cluster-expansion method that the 2D boron sheet is very likely to exhibit polymorphism, namely, multiple 2D structures with comparable stabilities.[37] In particular, they presented two new boron sheets that are predicted to be the ground-state structure for η = 1/8 and 2/15 group.[37] Hereafter, we

TABLE 1. Computed Cohesive Energy per Atom, η Values, Number of Boron Atoms per Unit Cell (n), and Ratios of Number of Atoms with CN = 4, 5, 6 for (a) δ-, χ-, and ψ-Type and (b) α- and β-Type Boron Monolayer Sheets (see Figure S1) (Greatest Cohesive Energy in PBE and PBE0 Calculations Is Highlighted in Bold)

(a)

boron sheet	E_c (PBE)	η	n	ratios of CN (4:5:6)
δ_3	4.877	1/3	2	
δ_4	5.384	1/4	3	
δ_5 (ref 34)	5.684	1/7	6	
δ_6 (buckled)	5.662	0	1	
χ_1	5.740	3/17	14	2:5:0
χ_2	5.740	1/6	10	1:4:0
χ_3	5.723	1/5	4	1:1:0
χ_4	5.660	1/6	10	1:4:0
χ_5	5.638		6	1:2:0
ψ	5.483	1/4	6	

(b)

boron sheet	E_c (PBE)	E_c (PBE0)	η	n	ratios of CN (4:5:6)
α (ref 34)	5.760	5.582	1/9	8	0:3:1
α' (buckled)	**5.762**	5.619	1/9	8	0:3:1
α_1	5.732	**5.718**	1/8	14	0:6:1
α_2	5.744	5.581	1/8	14	0:6:1
α_3	5.735	5.528	1/9	8	0:3:1
α_4	5.696		1/11	10	0:3:2
α_5 (ref 34)	5.629		1/12	11	0:6:5
β (ref 34)	5.651	5.560	1/8	7	2:2:3
β_1	5.746	**5.678**	1/8	14	1:4:2
β_2 (buckled)	5.743	5.649	1/7	12	1:4:1
β_3 (buckled)	5.737	5.639	1/6	10	2:2:1
$g_{1/8}$ (β_4) (ref 37)	5.747	5.617	1/8	21	2:5:14
$g_{2/15}$ (β_5) (ref 37)	5.740	5.612	2/15	26	2:3:8
β_6	5.734	5.600	1/6	10	2:2:1
β_7	5.736	5.573	1/7	12	1:4:1
β_8	5.724		1/9	8	1:1:2
β_9	5.719		1/6	12	1:10:1
β_{10}	5.718		1/8	7	2:2:3
β_{11}	5.712		1/6	10	3:6:1
β_{12} (ref 36; original γ-sheet)	5.712		1/6	5	2:2:1
β_{13}	5.702		1/6	10	2:2:1

name the two new ground-state boron sheets as $g_{1/8}$- and $g_{2/15}$-sheets. The aim of this study is to utilize first-principles-based global research to seek new lowest-energy polymorphs of the 2D boron sheets. Our search yields two highly stable boron monolayer sheets, namely, α_1-sheet and β_1-sheet, both with a value of η = 1/8. The two boron monolayers possess greater cohesive energies (by more than 60 meV/atom based on structural optimization using the PBE0 hybrid functional) than the α-sheet previously predicted by Tang and Ismail-Beigi[33,34] and the $g_{1/8}$- and $g_{2/15}$-sheets (both belonging to the β-type) recently reported by Yakobson and co-workers.[37]

RESULTS AND DISCUSSION

The η parameter defined above is a global structural parameter to describe area density of hexagon holes. In addition, a local structural parameter, that is, the coordination number (CN) of boron atoms is used here to classify boron monolayer sheets into various types, such as (1) α-type, CN = 5, 6; (2) β-type, CN = 4, 5, 6; (3) χ-type, CN = 4, 5; (4) ψ-type, CN = 3, 4, 5; and (5) δ-type, a single value of CN. For example, a buckled triangle sheet has CN = 6, hence named as δ_6-sheet; the graphene-like honeycomb sheet has CN = 3, hence named as δ_3-sheet (Figure 1a). Overall, 9000 boron sheet structures are generated from the structural search based on the PSO algorithm. In Table 1, we list the calculated cohesive energies per atom E_c (PBE and PBE0), η values, number of boron atoms per unit cell n, and ratios in number of atoms with CN = 4, 5, 6 for the low-energy boron monolayer sheets studied.

δ-Type and χ-Type Boron Sheets. In Figure 1a, δ_4- and δ_5-sheets are also plotted; the former has a value of η = 1/4 and is structurally identical to the B_2C sheet reported previously,[38] while the latter is previously named as the B(1/7) sheet[33,34] with a value of η = 1/7. The honeycomb δ_3-sheet has the smallest cohesive energy of 4.877 eV (in PBE calculation, consistent with previous PBE calculation[39]), indicating that the graphene-like structure is energetically unfavorable for boron. The buckled triangular δ_6-sheet is more stable than δ_3-sheet and δ_4-sheet (see Table 1a). The δ_5-sheet has the greatest cohesive energy among the four δ-type sheets, and it is planar, implying that boron atoms with CN = 5 are likely prevailing in low-energy boron sheets. Previous theoretical studies have shown that some boron sheets such as δ_6-sheet are buckled due to the $\sigma-\pi$ mixing,[33,34] while others such as δ_3- and δ_5-sheets prefer planar (unbuckled) shape.

For the χ-type sheets (Figure 1b and Figure S2 in the Supporting Information), boron atoms have CN of either 4 or 5. The χ_1-sheet appears to be the most stable among the four χ-type sheets (Table 1a). Although χ_3-sheet has the largest fraction of boron atoms with CN = 5, and χ_2-sheet has the least fraction of boron atoms with CN = 4; both sheets are energetically less favorable than the χ_1-sheet, suggesting that an optimal mix of boron atoms with CN = 4 and 5 would be energetically favorable.

Boron Sheets: α-Type. Boron atoms in α-type sheets (Figure 1c and Figure S1) have CN of either 5 or 6, and the sheets generally have greater cohesive energies than δ-type and χ-type sheets. Previously, it has been shown that the α-sheet[33,34] has the greatest cohesive energy based on PBE calculation (see Table 1b). However, as shown in Figure 2b, the calculated phonon spectrum of the α-sheet exhibits negative phonon frequencies. The largest negative frequency amounts to about -72 cm^{-1} near the M(0.5 0.0 0.0) k-point.

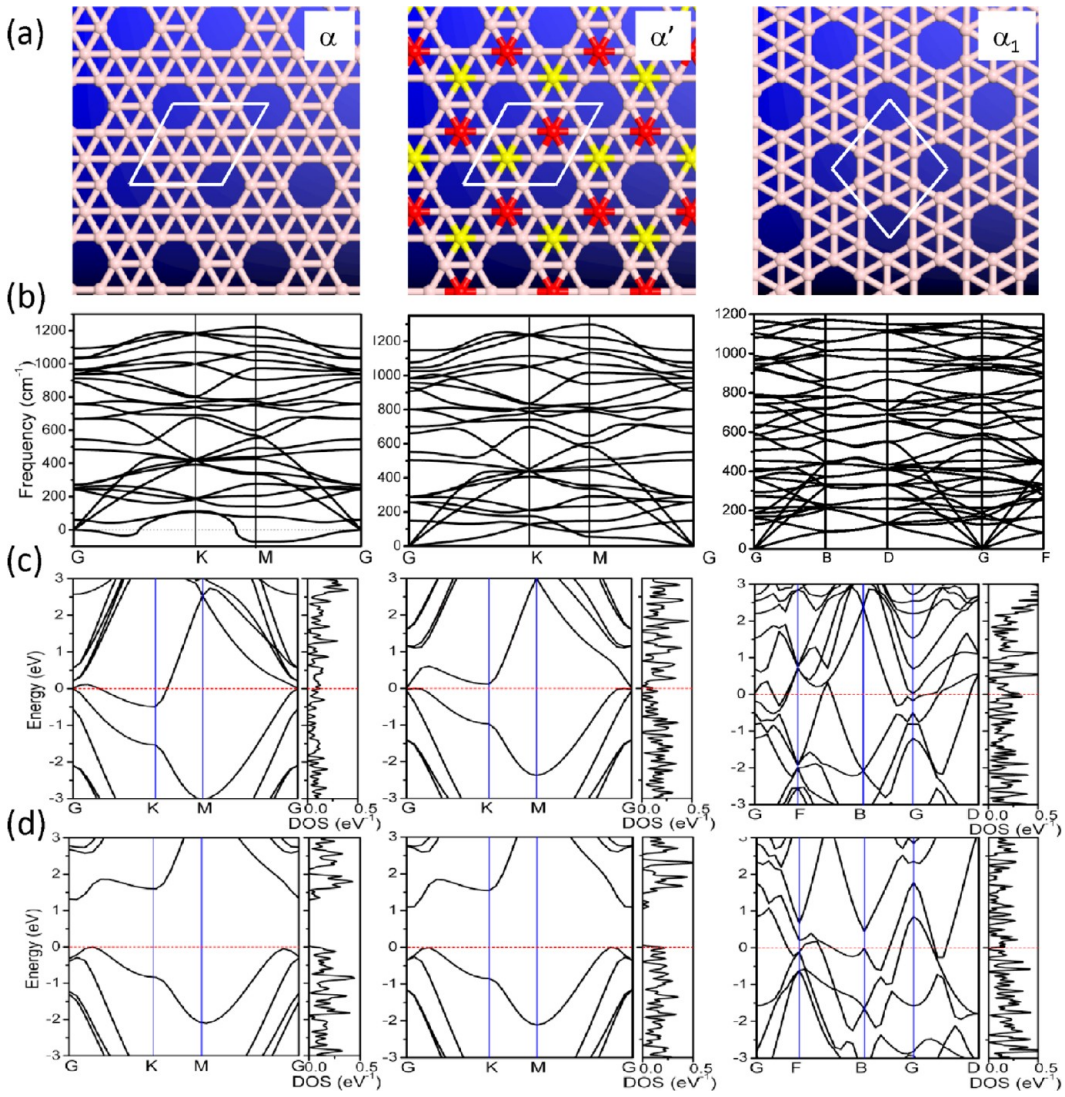

Figure 2. (a) Top view of α-, α′-, and α_1-sheets. (b) Calculated phonon spectra for α-, α′-, and α_1-sheets. Calculated electronic band structures of α-, α′-, and α_1-sheets, based on (c) PBE and (d) PBE0 calculation. The Fermi energy is set as zero. G, K, M(F), B, and D correspond to the (0, 0, 0), (−0.333, 0.667, 0), (0, 0.5, 0), (0.5, 0, 0), and (0.5, 0.5, 0) *k*-points, respectively, in the first Brillouin zone.

The eigenvectors of the negative frequency mode manifest an out-of-plane bending vibration. After new structural relaxation to remove the negative frequencies, the α-sheet becomes slightly buckled, hereafter named the α′-sheet. As shown in Table 1b, the α′-sheet has a greater cohesive energy than the α-sheet based on PBE and PBE0 calculations. In the α′-sheet, every two adjacent boron atoms with CN = 6 move inward and outward from the plane, and the vertical distance from the plane is about ±0.17 Å. Due to the weak buckling, the lattice constants *a* and *b* of the α′-sheet (5.046 and 5.044 Å) are slightly smaller than those of the α-sheet (5.050 and 5.050 Å). The α-sheet has received much attention not only because it has been the best candidate for the lowest-energy boron monolayer sheet but also because its structure is closely related to the boron buckyball B_{80}.[18−22] It is also noteworthy that although the calculated band structure and density of state (DOS) based on PBE functional suggest that α- and α′-sheets are metallic (Figure 2c), the hybrid PBE0 calculation suggests that both α- and α′-sheets are semiconducting with an indirect band gap of 1.40 and 1.1 eV, respectively (Figure 2d).

It is well-known that DFT in GGA functionals (such as the PBE functional) tend to underestimate the energy gaps. Specifically, several small band gap semiconductors, such as Ge, GaSb, InN, InAs, and InSb, are predicted to be quasi-metallic on the basis of the PBE functional.[40] This has been attributed to their inherent lack of derivative discontinuity[41] and to the delocalization error.[42] Much effort has been devoted to resolve this band gap problem, such as using the GW approximation,[43] time-dependent DFT,[44] exact exchange,[45] hybrid and screened hybrid functionals,[46−48] or modified Becke−Johnson potentials.[49] Although the PBE0 result of α-sheet differs from previously reported results in trend,[33,34,37]

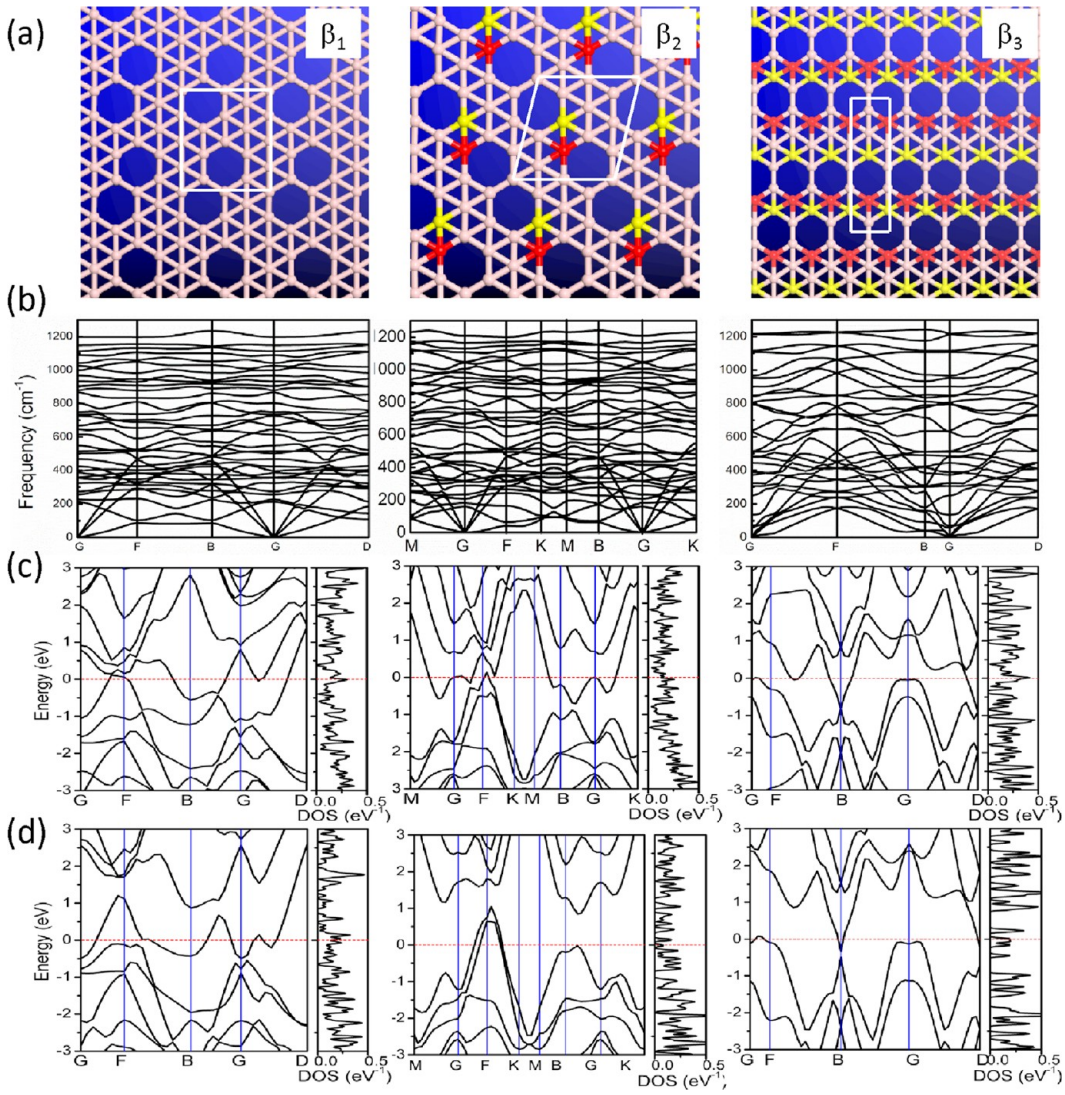

Figure 3. (a) Top view of β_1-, β_2-, and β_3-sheets. (b) Calculated phonon spectra for β_1-, β_2-, and β_3-sheets. Calculated electronic band structures of β_1-, β_2-, and β_3-sheets, based on (c) PBE and (d) PBE0 calculation. The Fermi energy is set as zero. G, K, M, F, B, and D correspond to the (0, 0, 0), (0.590, 0.400, 0), (0.410, 0.600, 0.0), (0, 0.5, 0), (0.5, 0, 0), and (0.5, 0.5, 0) *k*-points in the first Brillouin zone, respectively.

it is believed that the PBE0 results should be more reliable than the PBE since the description of band gap from PBE0 has been proven to be more reliable than the PBE.[50,51] Therefore, α- or α′-sheet is more likely to be small gap semiconductor rather than a metal. In addition to the α-sheet, our structural search also yields several low-energy structures that belong to α-type. The top three lowest-lying structures are within 40 meV (in PBE calculation) in cohesive energy from the α-sheet and are named as α_1-, α_2-, and α_3-sheet (see Table 1b). More importantly, α_1-sheet, with a value of $\eta = 1/8$, gives rise to the greatest cohesive energy based on the PBE0 calculation, greater than those of the α-sheet[31] and the two new boron sheets recently reported by Yakobson and co-workers[37] (Table 1b). Since the PBE0 hybrid functional has been reported to be more reliable than the PBE functional for computing cohesive energy of bulk materials,[50,51] the predicted relative stabilities are entirely based on the PBE0 results rather than the PBE results.

As indicated by Tang and Ismail-Beigi[33,34] and confirmed by Yakobson and co-workers,[37] boron sheets with high stability should have the Fermi level located within the gap of the in-plane derived projected density of states (PDOS). As such, all of the in-plane bonding states are filled, while none of the antibonding ones is filled. In Figure S2a, we plot the in-plane and out-of-plane derived PDOS for α_1-sheet. Indeed, one can see that the system is characterized by metallic p_z-derived band; specifically, the Fermi level lies within the gap of in-plane PDOS, consistent with the conclusion mentioned above, indicating that the α_1-sheet is possibly a boron sheet with the highest stability. Figure S3 displays the computed iso-surface of charge density for the topmost and the second topmost valence bands that cross the Fermi level of the α_1-sheet.

The morphology of the iso-surface is consistent with the band structure calculation in that the α_1-sheet is metallic.

A special structural feature of α_1-sheet is that every center-occupied hexagon is isolated from each other. As such, α_1-sheet is perfectly flat. As shown in Figure 2b, the calculated phonon spectrum of the α_1-sheet indicates that this new 2D crystalline structure of boron is stable without showing dynamical instabilities (negative frequencies). The highest optical phonon at Γ point for α_1-sheet corresponds to a B−B stretching mode with a frequency of 1167 cm^{-1}, an indication of relatively strong B−B bonding. As a comparison, the same phonon frequency is 1148 cm^{-1} for α'-sheet. This slightly lower frequency is consistent with slightly longer B−B bonds in α'-sheet due to buckling. Calculated electronic band structures and DOS of α_1-sheet based on both PBE and PBE0 functionals are shown in Figure 2c,d, which show that α_1-sheet is metallic. In summary, the newly predicted α_1-sheet is planar and metallic, and it is a leading candidate for the most stable planar (or locally unbuckled) boron sheet; weakly buckled α'-sheet is predicted to be semiconducting and possibly is the best candidate for the most stable buckled boron sheet.

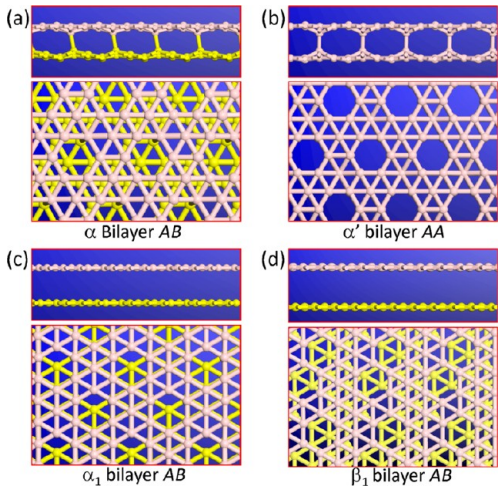

Figure 4. Side and top view of bilayer α'-sheet in (a) AA and (b) AB stacking, (c) bilayer α_1- and (d) bilayer β_1-sheets. Bilayer α'-sheet shows interlayer covalent bonds in either AB or AA stacking. The two monolayer β_1-sheets become weakly buckled when forming the bilayer. The interlayer distance for bilayer α'-sheet ranges from 1.87 to 3.38 Å in AB stacking and from 1.82 to 3.51 Å in the AA stacking. The interlayer distances for planar bilayer α_1-sheet and β_1-sheet are 3.62 and 3.66 Å, respectively. Yellow balls in (a), (c), and (d) represent the bottom layer.

Boron Sheets: β-Type. Boron atoms in β-type sheets (Figure 1d and Figure S1) have CN of 4, 5, and 6. As a result, much richer structures of β-type sheets are obtained than δ-, χ-, and α-type sheets. The first (and original) β-sheet was reported by Tang and Ismail-Beigi.[33,34] Later, Boustani and co-workers[36] reported a more stable β-type sheet, previously named as the γ-sheet (or β_{10}-sheet in this study; see Table 1b). Our extensive structural search yields nine new low-energy β-type sheets, all having greater cohesive energies than both the original β- and γ-sheets. As shown in Table 1b, their relative stabilities depend strongly on the ratios of CN (4:5:6). In Figure 3a, the top three lowest-energy sheets, named β_1-, β_2-, and β_3-sheet, are plotted. Calculated phonon spectra of β_1-, β_2-, and β_3-sheets are plotted in Figure 3b, showing that all three sheets are stable without giving any negative frequencies. The β_1-sheet is predicted to be planar, and it possesses the second greatest cohesive energy based on PBE0 calculation (Table 1b). To confirm high

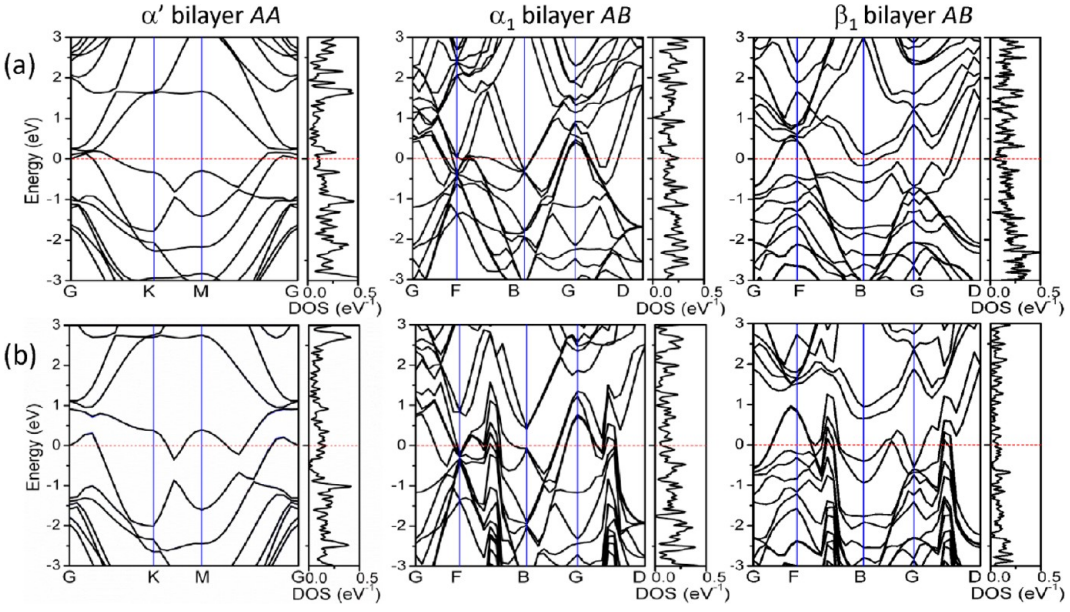

Figure 5. Computed band structures and density of state based on (a) PBE and (b) PBE0 calculation for bilayer α'-, α_1-, and β_1-sheets. The *k*-point lines are the same as those in Figures 2 and 3.

stability of the β_1-sheet, we also plot the in-plane and out-of-plane derived PDOS in Figure S2b. Again, one can see the Fermi level falling within the gap of in-plane derived PDOS, implying that the β_1-sheet is also a promising candidate for the lowest-energy boron sheet. Note that β_2- and β_3-sheets are slightly buckled. In the β_2-sheet, two adjacent boron atoms with CN = 5 move inward and outward from the sheet plane, and the vertical distance from the plane is about $\pm$0.048 Å, smaller in magnitude than that of the α'-sheet. Calculated electronic band structures and DOS of the β_1-, β_2-, and β_3-sheets based on both PBE and PBE0 functionals are shown in Figure 3c,d, and both calculations suggest that β_1-, β_2-, and β_3-sheets are all metallic. In summary, β_1-sheet is predicted to be another leading candidate for the most stable planar boron sheet, while the β_2- and β_3-sheets are predicted to be two additional promising candidates for the most stable buckled boron sheet.

The $g_{1/8}$- and $g_{2/15}$-sheets recently reported by Yakobson and co-workers[37] also belong to the β-type. On the basis of the PBE0 calculations, the cohesive energy per atom of the two sheets is ranked no. 4 and no. 5, respectively (Table 1b). The calculated electronic band structures and DOS of the $g_{1/8}$- and $g_{2/15}$- (or β_4- and β_5-) sheets are shown in Figure S2, and their phonon spectra are shown in Figure S4. Both PBE and PBE0 calculations suggest that $g_{1/8}$- and $g_{2/15}$-sheets are metallic, consistent with previous calculations.[37]

Bilayer α-, α′-, α_1-, and β_1-Sheets: Interlayer Distance and Bonding. Interlayer distance of a bilayer can be a measure of interlayer interaction and also used for assessing the tendency of buckling. A buckled sheet typically entails stronger interlayer interaction than an unbuckled sheet. Figure 4a–d displays both side and top views of geometrically optimized bilayer α′-, α_1-, and β_1-sheets. For geometric optimization of the three bilayers, the initial interlayer distance is set greater than 3.1 Å. A DFT method including dispersion correction (DFT-D2) is employed to account for the weak vdW interaction between two monolayer sheets (see Computational Methods section). For α′-sheet, covalent-like B–B bonds are formed between two α′-sheets. Two stacking patterns for bilayer α′-sheet are considered, namely, the AA stacking (Figure 4a) and AB stacking (Figure 4b). The AB stacking is similar to bilayer graphene where the center of empty hexagons in one layer is located on top of the center of filled hexagon of the opposing layer. For bilayer α′-sheet, the AB stacking is energetically less favorable than the AA stacking by 4 meV per supercell (in PBE calculation). The interlayer binding energy amounts to 0.145 eV/atom for the AA stacking. The shortest and largest B–B distances between two opposing α′-monolayer are 1.82 and 3.51 Å, respectively.

Like the monolayer α_1-sheet, the bilayer α_1-sheet is flat, as well. Only the AB stacking is found to be stable, with optimal interlayer distance being 3.62 Å, as shown in Figure 4c. Note that this optimal distance is close to the measured interlayer distance (~3.2 Å) in MWBNTs.[31] The interlayer vdW interaction for bilayer α_1-sheet is ~57 meV/atom based on the DFT-D2 calculation. Lastly, bilayer β_1-sheet in the AB stacking is still planar with the interlayer distance being 3.66 Å, also close to the measured interlayer distance (~3.2 Å) in MWBNTs.[31]

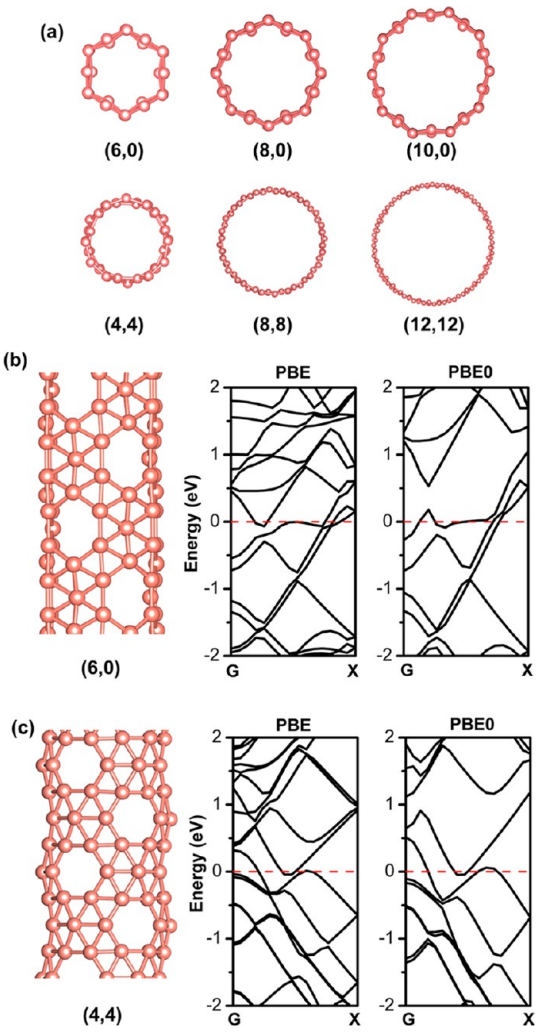

Figure 6. (a) Top view of a cross section of zigzag and armchair α_1-SWBNTs. (b,c) Side view of the geometric structure, as well as computed band structures of (6,0) and (4,4) α_1-SWBNTs, respectively. The band structures are computed based on both PBE and PBE0 functionals, using the CASTEP 6.0 program. The Fermi level is denoted with the red dashed line. G and X represent (0, 0, 0) and (0, 0, 0.5) *k*-points, respectively, in the first Brillouin zone.

Electronic band structures of three bilayers are shown in Figure 5, where the band structure of bilayers can be viewed as a combination of two constituent monolayer sheets. Note that the interlayer covalent B–B bonding of bilayer α′-sheet significantly changes the sheet's electronic properties. In fact, bilayer α′-sheet is predicted to be metallic (see Figure 5a,b), although monolayer α′-sheet is predicted to be semiconducting.

TABLE 2. Computed Diameter (D), Band Gap (E_{gap}; PBE Calculation for All and PBE0 Calculation for (4,4) and (6,0) Only), and Average Formation Energy per Atom (E_{form}) of Armchair and Zigzag α_1-SWBNTs (Number of Atoms per Unit Cell (n_c) Is Also Given)

SWBNT	D (Å)	band gap (eV)	E_{form} (eV/atom)	n_c
(4,4)	6.4	0, metal	0.113	42
(8,8)	13.3	0, metal	0.039	86
(12,12)	19.5	0, metal	0.032	126
(6,0)	5.9	0, metal	0.110	42
(8,0)	7.7	0, metal	0.069	56
(10,0)	9.9	0, metal	0.066	70

SWBNTs: Rolling up an α_1-Sheet. Like singled-walled carbon nanotubes (SWCNTs), SWBNTs can be also viewed as rolled-up boron monolayer sheets.[32−34] As a proof of principle, we construct several zigzag and armchair α_1-SWBNTs by rolling up the α_1-sheet in different ways, following the construction method of SWCNTs. Top and side views of optimized prototype zigzag and armchair α_1-SWBNTs are shown in Figure 6a,b, respectively. Interestingly, although α_1-sheet is a planar structure, its tubular structures are slightly buckled. Calculated electronic band structures of α_1-SWBNTs suggest that α_1-SWBNTs are all metallic, regardless of their diameter and chirality. This result is consistent with an experimental finding that as-produced MWBNTs are metallic.[30,31] Similar buckling behavior was also seen previously in α-SWBNTs. However, Singh *et al.* found that α-SWBNTs are no longer metallic but semiconducting if α-SWBNTs are buckled.[52] Since the α′-sheet is slightly buckled and is more stable than the α-sheet, it is more likely that α′-SWBNTs are also slightly buckled and are semiconducting. In Table 2, we present calculated formation energies of α_1-SWBNTs, defined as $E_{form} = E_{tube}/n_c - \mu_B$, where E_{tube} is the total energy per unit cell of α_1-SWBNT, n_c is the number of boron atoms in the unit cell, and μ_B is the average cohesive energy per atom of the α_1-sheet. The formation energies of α_1-SWBNTs decrease as their diameter increases, and the formation energies range typically from few tens to few hundreds of millielectronvolts per atom.

CONCLUSIONS

We have performed a first-principles-based global research of lowest-energy structures of the 2D boron sheets. Our search yields two highly stable boron monolayer sheets, namely, α_1-sheet and β_1-sheet, both with a value of $\eta = 1/8$. We utilize the PBE0 hybrid density functional since this functional has been proven to yield more accurate cohesive energies and qualitatively correct band structure for nonmetallic bulk materials than the conventional GGA/PBE functional.[50,51] Note that the PBE0 functional (see Computational Methods) can yield consistent relative stabilities among the low-energy neutral isomers of B_{20} (double-ring *versus* planar and compact structures) or anionic isomers of B_9^- as those predicted from the high-level coupled-cluster calculations,[29,53,54] whereas the popular B3LYP hybrid functional has been shown to be unreliable in predicting the relative stabilities for the boron clusters.[53,54] Interestingly, the B3LYP calculations still predict that α_1- or α_2-sheets are the two most stable boron sheets among the five low-energy sheets (see Table S2), consistent with PBE0 calculations. Another popular hybrid functional for computing band structures and band gap of bulk materials is the HSE06 functional.[47,48] Note also that the HSE06 functional is closely related to the PBE0 functional, for which the exchange terms are divided into a short-range and a long-range part. To minimize expensive calculations of the long-range Hartree−Fock (HF) exchange, the latter is replaced by a long-range PBE exchange term, $E_{xc}^{HSE} = E_x^{HF,SR}(\mu)/4 + 3 \times E_x^{PBE,SR}(\mu)/4 + E_x^{PBE,LR}(\mu) + E_C^{PBE}$, where the screened parameter μ = 0.207/Å is determined from benchmark tests of molecules and bulk materials.[47,48] Hence, we expect that relative stabilities predicted from the HSE06 calculation would be similar to those from the PBE0 calculation.

The present PBE0 calculation predicts that the α-sheet is a semiconductor, whereas the PBE calculation predicts it is a metal (the GGA/PBE calculation is known to underestimate the band gap of semiconductors). The PBE0 calculations also show that the α_1-sheet not only has greater cohesive energies than the α-sheet by more than 130 meV but also is more stable (by 100 meV) than the state-of-the-art $g_{1/8}$- and $g_{2/15}$-sheets. When building a bilayer with either the α- or α′-sheet (the weakly buckled α-sheet which itself is slightly more stable than α-sheet), the bilayer α- or α′-sheet exhibits covalent-like B−B bonding between two monolayers and thus becomes strongly buckled. However, the bilayer α_1-sheet remains flat with an interlayer distance of 3.62 Å, close to the measured interlayer distance (∼3.2 Å) of MWBNTs. The interlayer vdW coupling for the bilayer α_1-sheet is about 57 meV/atom, while interlayer interaction for the bilayer α′-sheet amounts to 14 meV/atom due to the formation of B−B bonds. Hence, it would be easier to separate the bilayer α_1-sheet into two monolayer sheets than to separate the bilayer α′-sheet. Our calculations suggest that α_1-sheet tends to form unbuckled or buckled MWBNTs when rolled up, while α′-sheets might form boron nanowires (BNWs) when rolled up. It is noteworthy that Liu *et al.* observed in their experiment that as-produced MWBNTs and BNWs actually coexisted together. Hence, this experiment already implied that 2D boron sheets tend to form polymorphs, consistent with the previous[37] and present theoretical studies. Finally, in view of the fact that the α_1-sheet, β_1-sheet, as well as the $g_{1/8}$- and $g_{2/15}$-sheets are all leading candidates for the lowest-energy structures and all

are predicted to be metallic, we speculate that the boron monolayer sheets, regardless of detained geometric structures, may find application such as specialized electrode in batteries or as lithium storage. This is because boron nanostructures are known to bind lithium stronger, compared to the carbon counterparts.

COMPUTATIONAL METHODS

Density Functional Theory Calculation. All cohesive energy data reported in this study are based on the first-principles calculations within the framework of spin-polarized plane-wave density functional theory (DFT), implemented in CASTEP 6.0 program.[55−59] The ultrasoft pseudopotentials[60] and the exchange-correlation functional in the form of Perdew−Burke−Ernzerhof (PBE)[61] within the generalized gradient approximation (GGA) are selected for structural optimizations of all boron sheets. The plane-wave cutoff is set to 500 eV. For geometric optimization, both lattice constants and positions of atoms are relaxed. Upon optimization, the forces on all atoms are less than 0.01 eV/Å and the criterion for total energy convergence is 5.0×10^{-6} eV/atom. The optimized lattice constants for boron sheets considered are summarized in Table S1 (see Supporting Information). The vacuum distance over any boron sheet in the supercell is set to be 30 Å. The Brillioiun zone is sampled using *k*-points with 0.02 $Å^{-1}$ spacing in the Monkhorst−Pack scheme.[62]

Relative stability and electronic band structures of top candidates of lowest-energy boron sheets are further examined using a spin-polarized hybrid functional PBE0,[63] as implemented in CASTEP 6.0. The PBE0 functional combines PBE functional with a predefined amount of exact exchange. For PBE0 calculation, the norm-conserving pseudopotential[64] is used and the plane-wave cutoff is set to be 489 eV. Because PBE0 calculation is computationally very demanding, compared to PBE calculation, only positions of all atoms are relaxed while the lattice constants of boron sheets are fixed to be those from the PBE calculation. The forces on all atoms are optimized to be less than 0.03 eV/Å, and the criterion for total energy convergence is 1.0×10^{-5} eV/atom. The Brillioiun zone is sampled using *k*-points with 0.05 $Å^{-1}$ spacing in the Monkhorst−Pack scheme.

For structural optimization of boron bilayers, a semiempirical dispersion correction, represented by the Tkatchenko−Scheffler (TS) scheme, is included to account for interlayer vdW interaction more accurately.[65] The cohesive energy of boron sheet is defined as $E_c = E$(B atom) − E(boron sheet)/*n*, where *E*(boron sheet) and *E*(B atom) are the total energy of the boron sheet per unit cell and a single B atom, respectively; *n* is the number of boron atoms in the unit cell.

Phonon Spectrum Calculation. Phonon spectra of several top candidates of boron sheets are computed based a DFT perturbation method with the linear response, implemented in the QUANTUM ESPRESSO package.[66] We did not choose the CASTEP 6.0 program for computing the phonon spectra because it is computationally much more demanding. Again, the PBE functional is used for the exchange-correlation energy functional. The valence-ion interaction is described by ultrasoft pseudopotentials. A plane-wave cutoff energy of 40 Ry and a charge density cutoff of 400 Ry are adopted for the structural optimization. For α-, α′-, and α_1-sheets, phonon frequencies are calculated on 9 × 9, 9 × 9, and 6 × 6 uniform electron momentum grids and 3 × 3, 3 × 3, and 3 × 3 phonon wavevector meshes, respectively.

Structural Searching. The particle-swarm optimization (PSO) method within the evolutionary algorithm, as implemented in CALYPSO code,[67] is used to search for low-energy 2D boron monolayer sheets. This method has successfully predicted new highly stable 2D structures of boron−carbon sheets,[68] as well as high-pressure phases of boron,[69] ice, and oxygen.[70,71] In our calculations, the population size is set to 50, and the number of generations is maintained to be 30. The required structure relaxations are performed using the PBE functional, as implemented in VASP 5.2[72,73] (note that the CALYPSO code has not been combined with the commercial CASTEP 6.0 program yet). Unit cells containing boron atoms of 4, 6, 8, 10, 12, and 14, respectively, are considered. Again, we note that the CALYPSO/VASP computation is merely to produce initial structures of boron monolayers (>9000 structures). Cohesive energies of all the low-energy boron structures are computed using the CASTEP 6.0 program.

Conflict of Interest: The authors declare no competing financial interest.

Acknowledgment. USTC group is supported by the National Basic Research Program of China (Nos. 2011CB921400, 2012CB922001), NSFC (Grant Nos. 11004180, 51172223), One Hundred Person Project of CAS, Shanghai Supercomputer Center, and Hefei Supercomputer Center. UNL group is supported by ARL (Grant No. W911NF1020099), NSF (Grant No. EPS-1010674), Nebraska Center for Energy Sciences Research, the Nebraska Research Initiative, and a grant from USTC for (1000Plan) Qianren-B summer research, and by the University of Nebraska's Holland Computing Center.

Supporting Information Available: Optimized structures of boron sheets, projected density of states for α_1 and β_1 boron sheets based on PBE0 calculation, phonon band structure of $g_{1/8}$ and $g_{2/15}$, charge density distribution of topmost valence bands, computed lattice constants, and crystalline structure files are collected. This material is available free of charge *via* the Internet at http://pubs.acs.org.

REFERENCES AND NOTES

1. Kroto, H. W.; Heath, J. R.; O'Brien, S. C.; Curl, R. F.; Smalley, R. E. C_{60}: Buckminsterfullerene. *Nature* **1985**, *318*, 162–163.
2. Iijima, S. Helical Microtubules of Graphitic Carbon. *Nature* **1991**, *354*, 56–58.
3. Novoselov, K. S.; Geim, A. K.; Morozov, S. V.; Jiang, D.; Katsnelson, M. I.; Grigorieva, I. V.; Dubonos, S. V.; Firsov, A. A. Two-Dimensional Gas of Massless Dirac Fermions in Graphene. *Nature* **2005**, *438*, 197–200.
4. Röthlisberger, U.; Andreoni, W.; Parrinello, M. Structure of Nanoscale Silicon Clusters. *Phys. Rev. Lett.* **1994**, *72*, 665–668.
5. Yoo, S.; Zhao, J. J.; Wang, J. L.; Zeng, X. C. Endohedral Silicon Fullerenes Si_N ($27 < N < 39$). *J. Am. Chem. Soc.* **2004**, *126*, 13845–13849.
6. Jackson, K. A.; Horoi, M.; Chaudhuri, I.; Frauenheim, T.; Shvartsburg, A. A. Unraveling the Shape Transformation in Silicon Clusters. *Phys. Rev. Lett.* **2004**, *93*, 013401.
7. Sun, Q.; Wang, Q.; Jena, P.; Rao, B. K.; Kawazoe, Y. Stabilization of Si_{60} Cage Structure. *Phys. Rev. Lett.* **2003**, *90*, 135503.
8. Saranin, A. A.; Zotov, A. V.; Kotlyar, V. G.; Kasyanova, T. V.; Utas, O. A.; Okado, H.; Katayama, M.; Oura, K. Ordered Arrays of Be-Encapsulated Si Nanotubes on Si(111) Surface. *Nano Lett.* **2004**, *4*, 1469–1473.
9. Bai, J.; Zeng, X. C.; Tanaka, H.; Zeng, J. Y. Metallic Single-Walled Silicon Nanotubes. *Proc. Natl. Acad. Sci. U.S.A.* **2004**, *101*, 2664–2668.
10. Bai, J.; Tanaka, H.; Zeng, X. C. Graphene-like Bilayer Hexagonal Silicon Polymorph. *Nano Res.* **2010**, *3*, 694–700.
11. Boustani, I. New Quasi-Planer Surfaces of Bare Boron. *Surf. Sci.* **1997**, *370*, 355–363.
12. Boustani, I. Towards Novel Boron Nanostructural Materials. *Chem. Modell.* **2011**, *8*, 1–44.
13. Zhai, H. J.; Kiran, B.; Li, J.; Wang, L. S. Hydrocarbon Analogues of Boron Clusters-Planarity, Aromaticity and Antiaromaticity. *Nat. Mater* **2003**, *2*, 827–833.
14. Zhai, H. J.; Alexandrova, A. N.; Birch, K. A.; Boldyrev, A. I.; Wang, L. S. Hepta- and Octacoordiante Boron in Molecular Wheels of Eight- and Nine Boron Clusters: Observation

and Confirmation. *Angew. Chem., Int. Ed.* **2003**, *42*, 6004–6008.
15. Huang, W.; Sergeeva, A. P.; Zhai, H. J.; Averkiev, B. B.; Wang, L. S.; Boldyrev, A. I. A Concentric Planer Doubly π Aromatic B_{19}^- Cluster. *Nat. Chem.* **2010**, *2*, 202–206.
16. Alexandrova, A. N.; Boldyrev, A. I.; Zhai, H. J.; Wang, L. S. All-Boron Aromatic Clusters as Potential New Inorganic Ligands and Building Blocks in Chemistry. *Coord. Chem. Rev.* **2006**, *250*, 2811–2866.
17. Galeev, T. R.; Chen, Q.; Guo, J. G.; Bai, H.; Miao, C. Q.; Lu, H. G.; Sergeeva, A. P.; Li, S. D.; Boldyrev, A. I. Deciphering the Mystery of Hexagon Holes in an All-Boron Graphene α-Sheet. *Phys. Chem. Chem. Phys.* **2011**, *13*, 11575–11578.
18. Szwacki, N. G.; Sadrzadeh, A.; Yakobson, B. I. B_{80} Fullerene: An *Ab Initio* Prediction of Geometry, Stability, and Electronic Structure. *Phys. Rev. Lett.* **2007**, *98*, 166804.
19. Szwacki, N. G. Boron Fullerenes: A First-Principles Study. *Nanoscale Res. Lett.* **2008**, *3*, 49–54.
20. Yan, Q. B.; Sheng, X. L.; Zheng, Q. R.; Zhang, L. Z.; Su, G. Family of Boron Fullerenes: General Constructing Schemes, Electron Counting Rule, and *Ab Initio* Calculations. *Phys. Rev. B* **2008**, *78*, 201401(R).
21. Sadrzadeh, A.; Pupysheva, O. V.; Singh, A. K.; Yakobson, B. I. The Boron Buckyball and Its Precursors: An Electronic Structure Study. *J. Phys. Chem. A* **2008**, *112*, 13679–13683.
22. Jin, P.; Hao, C.; Gao, Z. X.; Zhang, S. B.; Chen, Z. F. Endohedral Metalloborofullerenes $La_2@B_{80}$ and $Sc_3N@B_{80}$: A Density Functional Theory Prediction. *J. Phys. Chem. A* **2009**, *113*, 11613–11618.
23. Li, H.; Shao, N.; Shang, B.; Yuan, L. F.; Yang, J. L.; Zeng, X. C. Icosahedral B_{12}-Containing Core−Shell Structures of B_{80}. *Chem. Commun.* **2010**, *46*, 3878–3880.
24. Zhao, J. J.; Wang, L.; Li, F. Y.; Chen, Z. F. B_{80} and Other Medium-Sized Boron Clusters: Core−Shell Structures, Not Hollow Cage. *J. Phys. Chem. A* **2010**, *114*, 9969–9972.
25. Boustani, I. Systematic *Ab Initio* Investigation of Bare Boron Clusters: Determination of the Geometry and Electronic Structures of B_n (n=2−14). *Phys. Rev. B* **1997**, *55*, 16426–16438.
26. Boustani, I.; Quandt, A. Nanotubules of Bare Boron Clusters: *Ab Initio* and Density Functional Study. *Europhys. Lett.* **1997**, *39*, 527–532.
27. Kiran, B.; Bulusu, S.; Zhai, H. J.; Yoo, S.; Zeng, X. C.; Wang, L. S. Planar-to-Tubular Structural Transition in Boron Clusters: B_{20} as the Embryo of Single-Walled Boron Nanotubes. *Proc. Natl. Acad. Sci. U.S.A.* **2005**, *4*, 961–964.
28. Oger, E.; Crawford, N. R. M.; Kelting, P.; Weis, P.; Kappes, M. M.; Ahlrichs, R. Boron Cluster Cations: Transition from Planer to Cylindrical Structures. *Angew. Chem., Int. Ed.* **2007**, *46*, 8503–8506.
29. An, W.; Bulusu, S.; Gao, Y.; Zeng, X. C. Relative Stability of Planar *versus* Double-Ring Tubular Isomers of Neutral and Anionic Boron Cluster B_{20} and B_{20}^-. *J. Chem. Phys.* **2006**, *124*, 154310.
30. Ciuparu, D.; Klie, R. F.; Zhu, Y. M.; Pfefferle, L. Synthesis of Pure Boron Single Wall Nanotubes. *J. Phys. Chem. B* **2004**, *108*, 3967–3969.
31. Liu, F.; Shen, C. M.; Su, Z. J.; Ding, X. L.; Deng, S. Z.; Chen, J.; Xu, N. S.; Gao, H. J. Metal-like Single Crystalline Boron Nanotubes: Synthesis and *In Situ* Study on Electronic Transport and Field Emission Properties. *J. Mater. Chem.* **2010**, *20*, 2197–2205.
32. Bezugly, V.; Kunstmann, J.; Grundkötter-Tock, B.; Frauenheim, T.; Niehaus, T.; Cuniberti, G. Highly Conductive Boron Nanotubes: Transport Properties, Work Functions, and Structural Stabilities. *ACS Nano* **2011**, *5*, 4997–5005.
33. Tang, H.; Ismail-Beigi, S. Novel Precursors for Boron Nanotubes: The Competition of Two-Center and Three-Center Bonding in Boron Sheets. *Phys. Rev. Lett.* **2007**, *99*, 115501.
34. Tang, H.; Ismail-Beigi, S. First-Principles Study of Boron Sheets and Nanotubes. *Phys. Rev. B* **2010**, *82*, 115412.
35. Miller, J. New Sheet Structures May be the Basis for Boron Nanotubes. *Phys. Today* **2007**, *60*, 20–21.
36. Özdoğan, C.; Mukhopadhyay, S.; Hayami, W.; Güvenç, Z. B.; Pandey, R.; Boustani, I. The Unusually Stable B_{100} Fullerene, Structural Transitions in Boron Nanostructures, and a Comparative Study of α- and γ-Boron and Sheets. *J. Phys. Chem. C* **2010**, *114*, 4362–4375.
37. Penev, E. S.; Bhowmick, S.; Sadrzadeh, A.; Yakobson, A. I. Polymorphism of the Two-Dimensional Boron. *Nano Lett.* **2012**, *12*, 2441–2445.
38. Wu, X.; Pei, Y.; Zeng, X. C. B_2C Graphene, Nanotubes and Nanoribbons. *Nano Lett.* **2009**, *9*, 1577–1582.
39. Lau, K. C.; Pandey, R. Atomistically-Engineered 2D Boron Sheets. *J. Phys. Chem. C* **2007**, *111*, 2906–2912.
40. Heyd, J.; Peralta, J. E.; Scuseria, G. E. Energy Band Gaps and Lattice Parameters Evaluated with Heyd-Scuseria-Ernzerhof Screened Hybrid Functional. *J. Chem. Phys.* **2005**, *123*, 174101.
41. Sham, L. J.; Schlüter, M. Density-Functional Theory of the Energy Gap. *Phys. Rev. Lett.* **1983**, *51*, 1888–1891.
42. Mori-Sánchez, P.; Cohen, A. J.; Yang, W. Localization and Delocalization Errors in Density Functional Theory and Implications for Band-Gap Prediction. *Phys. Rev. Lett.* **2008**, *100*, 146401.
43. Hedin, L. New Method for Calculating the One-Particle Green's Function with Application to Electron-Gas Problem. *Phys. Rev.* **1965**, *139*, A796.
44. Runge, E.; Gross, E. K. U. Density-Functional Theory for Time-Dependent Systems. *Phys. Rev. Lett.* **1984**, *52*, 997–1000.
45. Städele, M.; Moukara, M.; Majewski, J. A.; Vogl, P.; Görling, A. Exact Exchange Kohn-Sham Formalism Applied to Semiconductors. *Phys. Rev. B* **1999**, *59*, 10031–10043.
46. Perdew, J. P.; Ernzerhof, M.; Burke, K. Rationale for Mixing Exact Exchange with Density Functionals Approximation. *J. Chem. Phys.* **1996**, *105*, 9982–9985.
47. Heyd, J.; Scuseria, G. E.; Ernzerhof, M. Hybrid Functionals Based on a Screened Coulomb Potential. *J. Chem. Phys.* **2003**, *118*, 8207–8215.
48. Heyd, J.; Scuseria, G. E.; Ernzerhof, M. Erratum: "Hybrid Functionals Based on a Screened Coulomb Potential". *J. Chem. Phys.* **2006**, *124*, 219906.
49. Tran, F.; Blaha, P. Accurate Band Gaps of Semiconductors and Insulators with a Semilocal Exchange-Correlation Potential. *Phys. Rev. Lett.* **2009**, *102*, 226401.
50. Paier, J.; Marsman, M.; Hummer, K.; Kresse, G.; Gerber, C. I.; Ángyán, J. G. Screened Hybrid Density Functionals Applied to Solids. *J. Chem. Phys.* **2006**, *124*, 154709.
51. Paier, J.; Marsman, M.; Kresse, G. Why Does the B3LYP Hybrid Functional Fail for Metals? *J. Chem. Phys.* **2007**, *127*, 024103.
52. Singh, A. K.; Sadrzadeh, A.; Yakobson, B. I. Probing Properties of Boron α-Tubes by *Ab Initio* Calculations. *Nano Lett.* **2008**, *8*, 1314–1317.
53. Li, F.; Jin, P.; Jiang, D.; Wang, L.; Zhang, S. B.; Zhao, J.; Chen, Z. F. B_{80} and $B_{101-103}$ Clusters: Remarkable Stability of the Core−Shell Structures Established by Validated Density Functionals. *J. Chem. Phys.* **2012**, *136*, 074303.
54. Pan, L.; Li, J.; Wang, L. S. Low-Lying Isomers of the B_9^- Boron Cluster: The Planar Molecular Wheel *versus* Three-Dimensional Structures. *J. Chem. Phys.* **2008**, *129*, 024302.
55. Hohenberg, P.; Kohn, W. Inhomogeneous Electron Gas. *Phys. Rev.* **1964**, *136*, B864–B871.
56. Kohn, W.; Sham, L. J. Self-Consistent Equations Including Exchange and Correlation Effects. *Phys. Rev.* **1965**, *140*, A1133–A1138.
57. Payne, M. C.; Teter, M. P.; Allan, D. C.; Arias, T. A.; Joannopoulos, J. D. Iterative Minimization Techniques for *Ab Initio* Total-Energy Calculations: Molecular Dynamics and Conjugate Gradients. *Rev. Mod. Phys.* **1992**, *64*, 1045–1097.
58. Clark, S. J.; Segall, M. D.; Pickard, C. J.; Hasnip, P. J.; Probert, M. J.; Refson, K.; Payne, M. C. First Principles Methods Using CASTEP. *Z. Kristallogr.* **2005**, *220*, 567–570.
59. Pfrommer, B. G.; Cote, M.; Louie, S. G.; Cohen, M. L. Relaxation of Crystals with the Quasi-Newton Method. *J. Comput. Phys.* **1997**, *131*, 233–240.
60. Vanderbilt, D. Soft Self-Consistent Pseudopotentials in a Generalized Eigenvalue Formalism. *Phys. Rev. B* **1990**, *41*, 7892–7895.

61. Perdew, J. P.; Burke, K.; Ernzerhof, M. Generalized Gradient Approximation Made Simple. *Phys. Rev. Lett.* **1996**, *77*, 3865–3868.
62. Monkhorst, H. J.; Pack, J. D. Special Points for Brillouin-Zone Integrations. *Phys. Rev. B* **1976**, *13*, 5188–5192.
63. Adamo, C.; Barone, V. Toward Reliable Density Functional Methods without Adjustable Parameters: The PBE0 Model. *J. Chem. Phys.* **1999**, *110*, 6158–6170.
64. Troullier, N.; Martins, J. L. Efficient Pseudopotentials for Plane-Wave Calculations. *Phys. Rev. B* **1991**, *43*, 1993–2006.
65. Tkatchenko, A.; Scheffler, M. Accurate Molecular van der Waals Interactions from Ground-State Electron Density and Free-Atom Reference Data. *Phys. Rev. Lett.* **2009**, *102*, 073005.
66. Giannozzi, P.; Baroni, S.; Bonini, N.; Calandra, M.; Car, R.; Cavazzoni, C.; Ceresoli, D.; Chiarotti, G. L.; Cococcioni, M.; Dabo, I.; *et al.* QUANTUM ESPRESSO: A Modular and Open-Source Software Project for Quantum Simulations of Materials. *J. Phys.: Condens. Matter.* **2009**, *21*, 395502/1–19.
67. Wang, Y. C.; Lv, J.; Zhu, L.; Ma, Y. M. Crystal Structure Prediction *via* Particle-Swarm Optimization. *Phys. Rev. B* **2010**, *82*, 094116.
68. Luo, X.; Yang, J.; Liu, H.; Wu, X. J.; Wang, Y. C.; Ma, Y. M.; Wei, S. H.; Gong, X. G.; Xiang, H. J. Predicting Two-Dimensional Boron−Carbon Compounds by Global Optimization Method. *J. Am. Chem. Soc.* **2011**, *133*, 16285–16290.
69. Oganov, A. R.; Chen, J.; Gatti, C.; Ma, Y. Z.; Ma, Y. M.; Glass, C. W.; Liu, Z.; Yu, T.; Kurakevych, O. O.; Solozhenko, V. L. Ionic High-Pressure Form of Elemental Boron. *Nature* **2009**, *457*, 863–867.
70. Wang, Y. C.; Liu, H. Y.; Lv, J.; Wang, H.; Ma, Y. M. High Pressure Partially Ionic Phase of Water Ice. *Nat. Commun.* **2011**, *2*, 563.
71. Zhu, L.; Wang, Z.; Wang, Y. C.; Zou, G. T.; Mao, H.; Ma, Y. M. Spiral Chain O_4 Form of Dense Oxygen. *Proc. Natl. Acad. Sci. U.S.A.* **2012**, *3*, 751–753.
72. Kresse, G.; Furthmüller, J. Efficiency of *Ab Initio* Total Energy Calculations for Metals and Semiconductors Using a Plane-Wave Basis Set. *J. Comput. Mater. Sci.* **1996**, *6*, 15–50.
73. Kresse, G.; Furthmüller, J. Efficient Iterative Schemes for *Ab Initio* Total-Energy Calculations Using a Plane-Wave Basis Set. *Phys. Rev. B* **1996**, *54*, 11169–11186.